


Nonthermal superconductivity in photodoped multiorbital Hubbard systemsSujoy Ray,¹ Yuta Murakami²,¹ and Philipp Werner¹¹*Department of Physics, University of Fribourg, Fribourg-1700, Switzerland*²*Center for Emergent Matter Science, RIKEN, Wako, Saitama 351-0198, Japan* (Received 10 May 2023; revised 12 October 2023; accepted 25 October 2023; published 27 November 2023)

Superconductivity in laser-excited correlated electron systems has attracted considerable interest due to reports of light-induced superconducting-like states. Here we explore the possibility of nonthermal superconducting order in strongly interacting multiorbital Hubbard systems, using nonequilibrium dynamical mean field theory. We find that a staggered η -type superconducting phase can be realized on a bipartite lattice in the high photodoping regime, if the effective temperature of the photocarriers is sufficiently low. The η superconducting state is stabilized by Hund coupling—a positive Hund coupling favors orbital-singlet spin-triplet η pairing, whereas a negative Hund coupling stabilizes spin-singlet orbital-triplet η pairing.

DOI: [10.1103/PhysRevB.108.174515](https://doi.org/10.1103/PhysRevB.108.174515)**I. INTRODUCTION**

The study of nonequilibrium quantum systems has become a frontier topic of research in condensed matter physics and quantum field theory [1–4]. A particularly interesting topic is the exploration of hidden phases of matter [5,6], that is, long-lived metastable states which can only be accessed via a nonthermal pathway. In strongly correlated electron systems, which are often characterized by competing low-energy states [7], nonequilibrium protocols offer the intriguing opportunity to manipulate material properties [5,6,8–13] and to create novel states with nonthermal electronic orders [1,14–26]. A promising route for realizing such nonequilibrium states is laser driving. This allows one to create Floquet states [27,28] or photodoped states [29], which under suitable circumstances can favor electron pairing and superconductivity. In photodoped large-gap Mott insulators, the charge excitations survive for a long time [30–33]. Rather than relaxing back to a (heated) equilibrium state, the charge excitations thermalize within the Hubbard bands, resulting in the formation of a metastable nonthermal state which can be characterized by effective temperatures of the charge carriers.

A broad range of theoretical tools has been employed to simulate photoinduced nonequilibrium states [34–44]. One of the challenges in laser-driven systems is the heating effect, which tends to suppress the emergence of electronic orders. Sophisticated protocols have been developed to realize effectively cold metastable systems. Entropy cooling techniques [19,45] have proven useful in overcoming relaxation bottlenecks and enabled the preparation of effectively cold nonequilibrium states of photodoped Mott systems. Alternatively, such states can be realized by the coupling to suitable fermionic [46] or bosonic baths [38]. Both techniques have been successfully used to simulate nonthermal superconducting (SC) states in the single-band repulsive Hubbard model [19,21,47]. SC states with staggered order parameter can be stabilized over a wide photodoping region on bipartite lattices [21], while chiral SC order with a 120° phase twist has been induced on a triangular lattice [47]. Here, we extend these

studies to multiorbital Hubbard systems—more specifically the two-orbital model with strong repulsive interactions.

Nonthermal orders in the two-orbital repulsive Hubbard model have been previously studied. These investigations include nonthermal spin and orbital orders in the three-quarter filled (Kugel-Khomskii) model [16,48,49] and excitonic orders in the model with crystal field splitting [17]. A photoinduced enhancement of a spin-triplet pairing susceptibility has also been reported [50], but due to computational limitations, this study could not reach a cold enough state for symmetry breaking and it did not consider the staggered order that we will identify below as the dominant nonthermal phase.

Here, we employ the recently developed nonequilibrium steady state (NESS) technique [46] to explore the photodoped two-orbital repulsive Hubbard model. Such a photodoped steady state exhibits a nonthermal distribution of charge carriers, which is produced, for example, by a laser excitation. In a large-gap Mott insulator, the relaxation of photoexcited charge carriers across the gap can take a very long time. As a result, the system approaches a photodoped quasisteady state with thermal-like distributions within the Hubbard bands. Explicit real-time simulations of photodoped Mott states confirmed that, in the presence of a dissipation mechanism, the photodoped system indeed relaxes to such a steady state with well-defined effective temperatures of the charge carriers [51]. The NESS technique allows us to directly realize (stabilize) such a steady state and to systematically explore a large parameter space in terms of the doping level and effective temperature. Using this technique, we will demonstrate the emergence of nonthermal SC states which are specific to multiorbital systems.

The paper is structured as follows. In Sec. II, we define the model and the NESS setup. In Sec. III, we compute the susceptibility for uniform and staggered orbital-singlet/spin-triplet and orbital-triplet/spin-singlet pairing and map out nonequilibrium phase diagrams, while Sec. IV contains a conclusion. Technical aspects related to the mean-field and dynamical-mean-field calculations are discussed in the Appendices.

II. MODEL AND METHOD

We consider the two-orbital Hubbard model with Hamiltonian

$$\begin{aligned}
 H = & -t_{\text{hop}} \sum_{(ij),\sigma} \sum_{\alpha=1,2} c_{i,\alpha\sigma}^\dagger c_{j,\alpha\sigma} + U \sum_i \sum_{\alpha=1,2} n_{i,\alpha\uparrow} n_{i,\alpha\downarrow} \\
 & - \mu \sum_i \sum_{\alpha=1,2} (n_{i,\alpha\uparrow} + n_{i,\alpha\downarrow}) + (U - 2J) \sum_{i,\sigma} n_{i,1\sigma} n_{i,2\sigma} \\
 & + (U - 3J) \sum_{i,\sigma} n_{i,1\sigma} n_{i,2\sigma}
 \end{aligned} \quad (1)$$

on a bipartite lattice. Here, α and σ denote the orbital and spin indices, respectively, t_{hop} is the nearest neighbor hopping amplitude between sites i and j , U is the intraorbital Hubbard repulsion, J is the Hund coupling, and μ is the chemical potential. The equilibrium ground state of the half filled model at large U is a Mott insulator with antiferro spin ($J > 0$) or orbital ($J < 0$) order. Away from half filling, for $J > 0$, orbital-singlet spin-triplet superconductivity appears over a wide range of dopings between quarter filling ($n = 1/4$) and three-quarter filling ($n = 3/4$) [50,52,53] and it is interesting to ask if a nonthermal manifestation of this order exists.

To create an effectively cold photodoped state, we employ the NESS formalism [21,46], where the system is weakly coupled to cold fermion baths at each site. By choosing the densities of states (DOS) $\rho_b(\omega)$ and chemical potentials μ_b of these baths appropriately, we can inject (remove) electrons into (from) the upper (lower) Hubbard band and stabilize a photodoped state. Here, we use fermion baths with a semi-elliptic DOS with a coupling strength g . The hybridization function $D_b(\omega)$ of these baths is given by $D_b(\omega) = g^2 \rho_b(\omega) = \Gamma \sqrt{W_b^2 - (\omega - \omega_b)^2}$, where W_b denotes the half bandwidth, ω_b indicates the center of the energy spectrum of the bath and $\Gamma = g^2/W_b^2$ is a dimensionless coupling parameter. We use four fermion baths with $\omega_b = \pm U/2, \pm 3U/2$ and the same W_b and Γ for all fermion baths. The two baths with $\omega_b = \pm U/2$ are chosen to coincide with the lower and upper Hubbard bands to create a large population of triply occupied sites (triplons) and singly occupied sites (singlons). The other two baths, a completely empty one with $\omega_b = 3U/2$ and a completely filled one at $\omega_b = -3U/2$, are added to prevent the production of high-energy fully occupied (quadruplon) and empty (holon) states; see Fig. 1(a). (Partially filled subbands at $\omega \approx \pm 3U/2$ would correspond to some population of quadruplons and holons.) In this setup, by tuning three parameters—the chemical potential of the bath μ_b , temperature of the bath T_b , and coupling Γ —we can prepare a half-filled nonequilibrium state with a desired density of triplons and singlons and an effectively cold temperature. The parameter μ_b mainly controls the photodoping (density of charge excitations—here triplons and singlons), while the other two parameters Γ and T_b mainly control the effective temperature of the photodoped charge carriers. In all our calculations, $T_b = 0.01$ unless otherwise mentioned.

The NESS solution of the two-orbital Hubbard model is obtained on an infinitely connected Bethe lattice using nonequilibrium dynamical-mean-field theory (DMFT) [54] and a noncrossing approximation (NCA) impurity solver [55]. To study uniform or staggered SC orders, we use the Nambu-

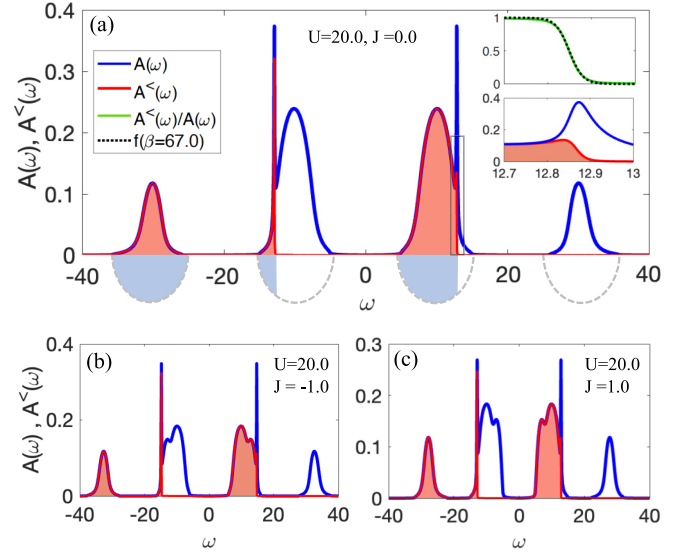


FIG. 1. Spectra of the photodoped two-orbital model with η superconducting order and with parameters (a) $U = 20$, $J = 0$, (b) $U = 20$, $J = -1$, and (c) $U = 20$, $J = 1$. The occupied DOS is indicated by the filled area. The four fermion baths and their occupations are indicated below the spectra in (a) by the gray dashed lines and filled blue areas, respectively. The insets in panel (a) show a zoom of the region indicated by the gray box and a fit to the Fermi distribution function with $\beta_{\text{eff}} = 67.0$ (black dashed line).

Keldysh formalism to write the DMFT self-consistency condition as $\Delta(t, t') = t_0^2 \gamma G(t, t') \gamma + D(t, t')$. Here, $t_0 = W/4$ is the quarter-bandwidth of the Bethe-lattice DOS, which is used as the unit of energy. The hybridization function Δ , impurity Green's function G , and hybridization function of the fermion baths $D = \sum_b D_b$ can be represented by matrices in the Nambu basis (see Appendix D), while the choice of the γ matrix determines whether the solution corresponds to staggered or uniform pairing [19].

In the calculations, we use $U = 20$, $J = \pm 1$, $\Gamma = 0.016\text{--}0.032$, and $W_b = 5$. The triplon density is measured as $\langle n_{1\uparrow} n_{1\downarrow} n_{2\uparrow} + n_{1\uparrow} n_{2\uparrow} n_{2\downarrow} - 4n_{1\uparrow} n_{1\downarrow} n_{2\uparrow} n_{2\downarrow} \rangle$, with $n_\alpha = n_{\alpha\uparrow} + n_{\alpha\downarrow}$ the occupation of orbital α . A typical spectral function $A(\omega)$ for a photodoped system with triplon density = 0.474 is shown in Fig. 1(a). The occupied density of states $A^less(\omega)$ is indicated by the filled area. An effective temperature T_{eff} of the system can be defined by comparing the ratio $A^less(\omega)/A(\omega)$ to a (shifted) Fermi distribution function $f_\beta(\omega)$ for inverse temperature β . The inset of Fig. 1(a) shows that $A^less(\omega)/A(\omega)$ can be very well fitted with $f_{\beta=67.0}(\omega)$, which indicates that the triplons (and singlons) in the nonequilibrium state have a well-defined and low effective temperature. We also see sharp quasiparticle peaks at the edges of the Hubbard bands, which are associated with the remaining doublon states. In equilibrium, at low temperature, a single doublon state dominates and the energy separation between the upper and lower Hubbard bands is roughly $U + J$ ($J > 0$) or $U - 5J$ ($J < 0$). In a photodoped system, all doublon states contribute to the spectrum, which exhibits peaks with a separation between $U - 5J$ and $U + J$. Hence, for $J > 0$ ($J < 0$), the separation between the Hubbard bands decreases (increases); see

Figs. 1(b), 1(c) and 7. A large enough gap ensures a slow relaxation across the gap [30,31] and is necessary for the stability of the photodoped state, which sets limits to the values of J .

III. RESULTS

In the two-orbital model we can define six types of SC orders, depending on the spin and orbital symmetry. The three orbital-singlet spin-triplet orders are measured by [52]

$$p_{i,sv} = \frac{1}{4} \sum_{\alpha\alpha'\sigma'} c_{i,\alpha\sigma}^\dagger \epsilon_{\alpha\alpha'} (\sigma^\nu \epsilon)_{\sigma\sigma'} c_{i,\alpha'\sigma'}^\dagger \quad (2)$$

and the three spin-singlet orbital-triplet orders by

$$p_{i,ov} = \frac{1}{4} \sum_{\alpha\alpha'\sigma'} c_{i,\alpha\sigma}^\dagger (\sigma^\nu \epsilon)_{\alpha\alpha'} \epsilon_{\sigma\sigma'} c_{i,\alpha'\sigma'}^\dagger, \quad (3)$$

where σ^ν denotes the three Pauli matrices with $\nu = x, y, z$ and the antisymmetric tensor is defined as $\epsilon = i\sigma^y$. In analogy to antiferromagnetic order in magnetically ordered systems, a staggered SC order (η order) can be defined, where $p_{i,\alpha}$ ($\alpha = sx, sy, sz, ox, oy, oz$) has opposite signs on the two sublattices A and B , such that

$$\eta_{i,\alpha}^+ = \delta_i^{A/B} p_{i,\alpha}, \quad (4)$$

with $\delta_i^{A(B)} = 1(-1)$ for i on the $A(B)$ sublattice.

Without Hund coupling, the local Hamiltonian is four-fold degenerate (spin degeneracy and orbital degeneracy) and at half filling, for sufficiently large U , each site is doubly occupied in the ground state. The photoexcitation creates singlon-triplon pairs. In the extreme photodoping limit, all doubly occupied sites are converted to singlons and triplons and, if the fluctuations between these states become large, we may expect the emergence of superconductivity with order parameters given by Eqs. (2) or (3), similar to the η pairing states in the photodoped single-band Hubbard model [19,21,23,25]. An important distinction however is that the triplons and singlons in the two-orbital model have spin and orbital degrees of freedom. The Hund coupling J lifts the degeneracy between the SC orders in the half filled system and favors a spin ($J > 0$) or orbital ($J < 0$) moment at each site. It also stabilizes the SC pairing, so that an η SC order can be realized at sufficiently large photodoping.

A. Effective model

Physical properties of photodoped states can be well captured by an effective model derived from the Schrieffer-Wolff transformation (SWT) or second order perturbation theory [21]. For $J = 0$ and half filling, the effective model for complete doping, where only triplons and singlons exist, can be derived by projecting the transformed Hamiltonian onto the singlon and triplon subspace as shown in Appendix A [56],

$$H_{\text{eff}} = H_{\text{hop}}^{st}/U + H_{\text{hop}}^{tt}/U + H_{\text{hop}}^{ss}/U, \quad (5)$$

where the low-energy effective interaction between triplons and singlons is divided into three terms representing the singlon-triplon, triplon-triplon, and singlon-singlon

interaction. Each term can be expressed in terms of spin, orbital, and η -spin operators as

$$H_{\text{hop}}^{st}/U = -\frac{4t_{\text{hop}}^2}{U} \sum_{\langle ij \rangle, \alpha} (\eta_{i\alpha}^+ \eta_{j\alpha}^- + \eta_{i\alpha}^- \eta_{j\alpha}^+) - \frac{4t_{\text{hop}}^2}{3U} \sum_{\langle ij \rangle} \left(\frac{1}{2} + 2s_i \cdot s_j \right) \left(\frac{1}{2} + 2\tau_i \cdot \tau_j \right), \quad (6)$$

$$H_{\text{hop}}^{ss}(tt) = \frac{2t_{\text{hop}}^2}{U} \sum_{\langle ij \rangle} \left(\frac{1}{2} + 2s_i \cdot s_j \right) \left(\frac{1}{2} + 2\tau_i \cdot \tau_j \right), \quad (7)$$

where $\eta_{i\alpha}^+$ is defined in Eq. (4), $\eta_{i\alpha}^-$ is the Hermitian conjugate $(\eta_{i\alpha}^+)^\dagger$, $s_i = \frac{1}{2} \sum_{\alpha} c_{i,\alpha\sigma}^\dagger \sigma_{\sigma\sigma'} c_{i,\alpha\sigma}$ is the spin moment, and $\tau_i = \frac{1}{2} \sum_{\alpha} c_{i,\alpha\sigma}^\dagger \sigma_{\alpha\alpha'} c_{i,\alpha\sigma}$ is the orbital moment. As can be seen from Eqs. (6) and (7), in addition to η -spin interaction terms, there are also spin interactions, orbital interactions, and spin-orbital composite terms. The temperature scales for all types of η orders are set by the coefficients which are $\sim t_{\text{hop}}^2/U$. Nonzero Hund coupling lifts the degeneracy between these η orders, because it affects the energies of the doublon states involved in the second order hopping processes. The exchange coupling for the η pairing channels α [the first term in Eq. (6)] is modified as $t_{\text{hop}}^2/U \rightarrow t_{\text{hop}}^2/\tilde{U}_\alpha$, where \tilde{U}_α is a function of U and J . $J > 0$ favors η_{sx} -type orbital-singlet spin-triplet order, while $J < 0$ favors η_{ox} -type orbital-triplet spin-singlet order (see Appendix A for a detailed discussion).

A mean-field (MF) decoupling may be applied to the effective model to obtain a MF Hamiltonian (see Appendix C). This MF calculation suggests that an η SC state can be achieved at low T_{eff} and that the Hund coupling enhances spin-triplet or orbital-triplet superconductivity, depending on J .

B. DMFT results

To detect a SC state, we apply a small seed field P_{seed} and couple it to the SC order we are interested in. For example, if we look for the p_{sx} SC order, we add the term $H_{\text{pair}} = P_{\text{seed}} \sum_i (p_{i,sx} + \text{H.c.})$ to the Hamiltonian (1) and measure the order parameter $\langle (p_{sx} + \text{H.c.}) \rangle$. For a η SC state, we use a staggered local seed field with opposite signs on the two sublattices and measure the SC order parameter $\langle \eta_\alpha^x \rangle$ and SC susceptibility χ_{SC} as

$$\langle \eta_\alpha^x \rangle = \text{Re}[\langle \eta_\alpha^+ \rangle] = \frac{\langle \eta_\alpha^+ + \eta_\alpha^- \rangle}{2}, \quad \chi_{SC} = \frac{\langle \eta_\alpha^x \rangle}{P_{\text{seed}}}. \quad (8)$$

This estimate works in the disordered state, not too close to the transition. In the symmetry-broken phase there is no linear relation between the order parameter and the applied seed field. In practice, however, a large value of the above ratio indicates an instability towards the superconducting phase. The effective temperature and band filling can be controlled by tuning the temperature and chemical potentials of the fermion baths, which allows us to map out the phase diagram of the nonequilibrium photodoped state in the space of triplon density and T_{eff} . For $J = 0$, all η pairing phases are degenerate and the highest transition temperature is $T_{\text{eff}} = 1/62.6$. A nonzero positive (negative) Hund coupling favors the spin triplet (orbital triplet) η phases and the corresponding transition temperatures increase.

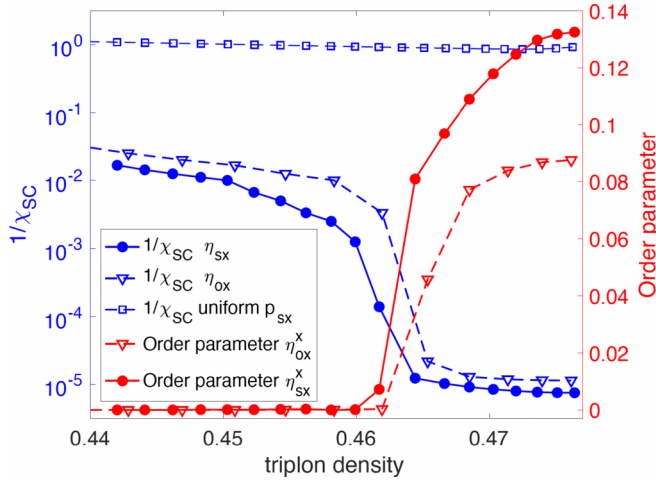


FIG. 2. SC order parameter η_{sx}^x , η_{ox}^x and inverse susceptibility $1/\chi_{SC}$ as a function of the triplon density for $U = 20$, $J = 1$, and $P_{seed} = 10^{-6}$. While χ_{SC} for η pairing is as high as 10^5 for large triplon densities, it remains of order 1 for uniform pairing. The effective temperature of the system is kept at $\beta_{eff} \approx 60.0$ by choosing $T_b = 0.01$ and $\Gamma = 0.02$.

Figure 2 plots the SC susceptibility χ_{SC} and order parameter $\langle \eta_{sx}^x \rangle$ as a function of the triplon density for $U = 20$ and $J = 1$. The η SC state appears at high triplon density ($\gtrsim 0.46$). When this long range order develops, the value of the order parameter becomes insensitive to the (small) seed field. On the other hand, χ_{SC} defined in Eq. (8) takes a large value, which scales $\propto 1/P_{seed}$. We observe an order parameter of the order of 10^{-1} , which for $P_{seed} = 10^{-6}$ corresponds to $\chi_{SC} \sim 10^5$. Importantly, this order parameter is almost unchanged if the seed is changed, which demonstrates that the order is due to a spontaneous symmetry breaking (see Appendix D). For comparison, we also plot in Fig. 2 the susceptibility for the uniform order p_{sx} , which remains small.

The β_{eff} vs triplon density phase diagram for the same interaction parameters is shown in Fig. 3. At half filling, without any photodoping, we have an antiferromagnetic (AFM) state, which is quickly suppressed with increasing triplon density. Over a wide region of intermediate photodopings, the system is in a normal paramagnetic state. As we approach the extreme doping limit, an η spin-triplet SC state is realized below a sufficiently low effective temperature ($\beta_{eff} \gtrsim 52.0$). Compared to the nonequilibrium DMFT results, the MF solution overestimates the SC transition temperature (red triangle in Fig. 3). This is because MF neglects temporal fluctuations. Moreover, the effective model H_{eff} , for which the MF solution is calculated, is valid only in the large- U limit, while the DMFT solution is affected by the bath couplings.

As mentioned earlier, in the two-orbital system there can be various SC orders with different spin and orbital symmetries. Thus, in Fig. 4, we also show the phase diagram for fixed $U = 20$ and $\beta_{eff} = 60$ in the space spanned by the triplon density and Hund coupling. The data for the orbital-triplet order η_{ox}^x and spin-triplet order η_{sx}^x , on which this phase diagram is based, are shown in the Fig. 9. Increasing $|J|$ favors the η SC order in both cases with a dominant η_{sx}^x pairing for positive J . Insights into the $J < 0$ case can be obtained by noting that

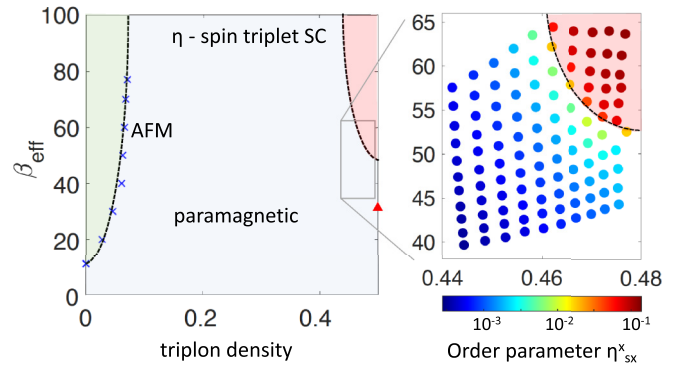


FIG. 3. Phase diagram of the two-orbital model with $U = 20$, $J = 1$, and $\Gamma = 0.02$ in the space of β_{eff} and triplon density. The AFM phase appears in the undoped and weakly photodoped region, while the η SC state is stabilized in the high photodoping region. The red triangle marks the MF transition temperature at triplon density 0.5. The right panel shows the color map of the order parameter $\text{Re}[\eta_{sx}^x]$ in the high photodoping region. Here, T_b and μ_b are varied to achieve different β_{eff} .

the $J > 0$ model can be mapped (qualitatively) to the $J < 0$ model by the transformations $c_{i,1\downarrow} \rightarrow c_{i,1\uparrow}$ and $c_{i,2\uparrow} \rightarrow c_{i,1\downarrow}$ [53]. This exchanges the roles of spin and orbital and it is thus natural that η_{ox}^x pairing becomes dominant for negative J . The smaller region of η_{ox}^x pairing compared to η_{sx}^x is due to the fact that the relevant interaction \tilde{U}_α is larger for $J < 0$ than for $J > 0$, which reduces the critical temperature ($\propto t_{hop}^2/\tilde{U}_\alpha$) for $J < 0$.

C. Optical conductivity

We finally calculate the optical conductivity and study how the optical response changes as we approach the SC phase from the normal phase. The steady state optical conductivity $\sigma(\omega)$ is calculated for the Bethe lattice from the local Green's function, following Ref. [21].

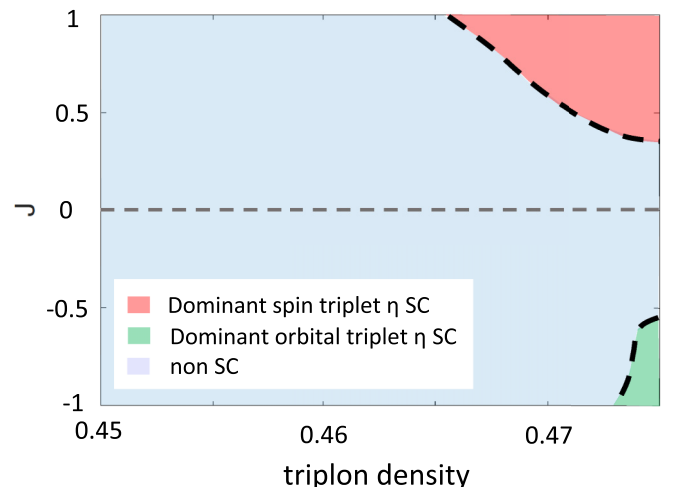


FIG. 4. Nonequilibrium phase diagram in the space of triplon density and Hund coupling J , for $U = 20$ and $\beta_{eff} = 60$.

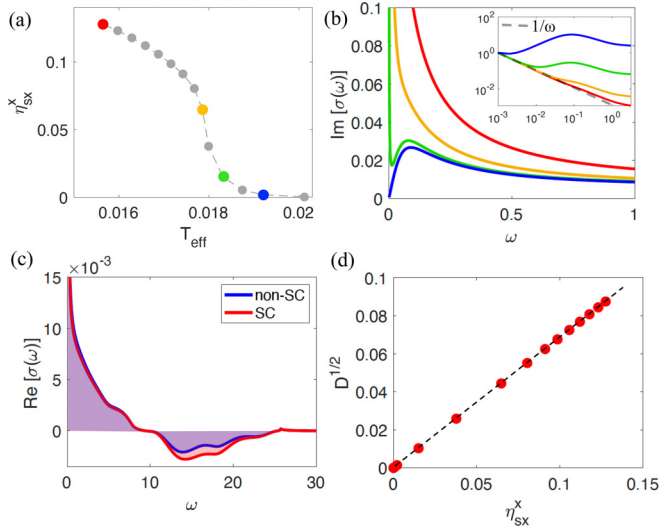


FIG. 5. Optical conductivity results for $U = 20$, $J = 1$ and for triplon density 0.473. (a) Order parameter η_{sx}^x as a function of effective temperature T_{eff} . (b) Imaginary part and (c) real part of the optical conductivity as a function of ω . The different colors in (b) and (c) correspond to the corresponding data points in (a). The inset of (b) shows the log-log plot of (shifted) $\text{Im}[\sigma(\omega)]$. (d) Square root of the SC phase stiffness D as a function of the order parameter η_{sx}^x .

Figure 5(a) shows the order parameter η_{sx}^x as a function of T_{eff} for the triplon density 0.473, $U = 20$, and $J = 1$. The SC transition temperature is $T_c \sim 0.019$. In both the normal and SC state, in addition to a narrow Drude peak, which we associate with the doublon population, the real part of $\sigma(\omega)$ shows a range of negative spectral weight around $\omega \sim 15$ [panel (c)]. The latter comes from triplon-singlon recombination processes in the population inverted nonequilibrium system, which are associated with local energy changes in the range from $U - 5J$ to $U + J$. The imaginary part, however, shows a distinct low-frequency behavior in the SC and non-SC states [panel (b)]. In the non-SC state (blue), $\text{Im}[\sigma(\omega)]$ decreases to 0 as $\omega \rightarrow 0$. The onset of superconductivity [green dot in panel (a)] is marked by a diverging $\text{Im}[\sigma(\omega)]$ as $\omega \rightarrow 0$, as shown by the green curve in panel (b). All the states which have a lower T_{eff} than this state, and hence are superconducting, exhibit a $1/\omega$ divergence at low ω . The inset of Fig. 5(b) shows the log-log plot of appropriately shifted $\text{Im}[\sigma(\omega)]$ and we can clearly observe the $1/\omega$ behavior below $\omega \approx 10^{-1}$ for the SC states (red and yellow). As T_{eff} increases, the energy region over which the $1/\omega$ scaling can be observed decreases and eventually disappears in the non-SC state (blue). We note that all the curves in Fig. 5(b) show an approximate power-law decay for $\omega > 10^{-1}$. However, the normal state behavior is different from a $1/\omega$ decay, as can be seen from the inset. The $1/\omega$ scaling at low frequencies thus provides evidence for the realization of a nonthermal SC state.

The $1/\omega$ divergence of $\text{Im}[\sigma(\omega)]$ allows us to define the SC phase stiffness D from the relation

$$\lim_{\omega \rightarrow 0} \text{Im}[\sigma(\omega)] = \frac{D}{\omega}.$$

In Fig. 5(d) we plot \sqrt{D} as a function of the order parameter η_{sx}^x for fixed $U = 20$, $J = 1$ and observe a linear scaling. This $D \propto |\eta|^2/U$ scaling is reminiscent of the two-fluid model for photodoped one-band Hubbard systems and holds in the entire SC region [21].

IV. CONCLUSIONS

We demonstrated that, upon photodoping, staggered η SC states can be realized in a small region near triplon density 0.5 in the half filled two-orbital repulsive Hubbard model. Unlike in the single-band model, the relevant local states have spin and orbital degrees of freedom, which potentially allows to realize different SC states. We showed that a positive Hund coupling enhances orbital-singlet spin-triplet η SC pairing, whereas a negative Hund coupling favors orbital-triplet spin-singlet η pairing. Due to the large U needed to stabilize the nonequilibrium states, the highest T_{eff} for realizing multi-orbital η pairing states are about an order of magnitude lower than in the single-band case [21]. However, in the realistic case where the energy unit is ~ 0.5 eV, the SC state can still be realized up to high effective temperatures of about 100 K. A possible material to search for orbital-singlet spin-triplet η pairing states is NiO, which is a Mott insulator with $J > 0$ that is often described by a half filled two-orbital Hubbard model. It will also be interesting to explore if similar η pairing states exist in photodoped three- or five-orbital systems and to check if SC states coexisting with spin or orbital orders can be realized.

ACKNOWLEDGMENTS

We thank J. Li and M. Eckstein for providing their NESS DMFT solver and J. Li and S. Hoshino for helpful discussions. The calculations have been run on the beo05 and beo06 clusters at the University of Fribourg. We acknowledge support from ERC Consolidator Grant No. 724103 and from SNSF Grant No. 200021-196966, and Grant-in-Aid for Scientific Research from JSPS, KAKENHI Grants No. JP20K14412, No. JP21H05017 (Y.M.), and JST CREST Grant No. JP-MJCR1901 (Y.M.).

APPENDIX A: SCHRIEFFER-WOLFF TRANSFORMATION

Here we sketch the derivation of the effective Hamiltonian used in the main manuscript for the photodoped two orbital repulsive Hubbard model. We focus on the effective Hamiltonian projected onto the triplon (triplly occupied sites) and singlon (singly occupied sites) subspaces. A detailed derivation and more general analysis can be found in Ref. [56]. We start with the two-orbital Hubbard model with Hund coupling given in Eq. (1). Our main objective is to get an effective low-energy Hamiltonian for high U (strong coupling limit) and to project the effective Hamiltonian to different occupation number sectors for nearest neighbor sites i and j .

First, we consider the case without Hund coupling ($J = 0$) and perform a generalized Schrieffer-Wolff transformation (SWT) using a rotating-frame time evolution [56]. We define

the projected operators (or Hubbard operators) from the creation and annihilation operators as

$$c_{i,\alpha\sigma}^\dagger = \sum_{n=1}^4 P_{i,n} c_{i,\alpha\sigma}^\dagger = \sum_{n=1}^4 \tilde{c}_{i,\alpha\sigma,n}^\dagger, \quad (\text{A1})$$

$$c_{i,\alpha\sigma} = \sum_{n=1}^4 c_{i,\alpha\sigma} P_{i,n} = \sum_{n=1}^4 \tilde{c}_{i,\alpha\sigma,n}, \quad (\text{A2})$$

where $P_{i,n}$ is the projector to the states at site i with n particles. Hence $\tilde{c}_{i,\alpha\sigma,n}^\dagger$ creates a particle in orbital α and with spin σ at site i , resulting in a state with n particles at site i . Similarly, $\tilde{c}_{i,\alpha\sigma,n}$ annihilates a particle at site i in a state that has n particles. Alternatively, these operators can also be written as $\tilde{c}_{i,\alpha\sigma,n}^\dagger = c_{i,\alpha\sigma}^\dagger P_{i,n-1}$ and $\tilde{c}_{i,\alpha\sigma,n} = P_{i,n-1} c_{i,\alpha\sigma}$. With the introduction of these projected operators, the kinetic (hopping) term can be written as

$$H_{\text{hop}} = \sum_{n,n'} H_{\text{hop},nn'}, \quad (\text{A3})$$

where $H_{\text{hop},nn'}$ is given by

$$\begin{aligned} H_{\text{hop},nn'} &= -t_{\text{hop}} \sum_{(ij)} \sum_{\alpha\sigma} \tilde{c}_{i,\alpha\sigma,n}^\dagger \tilde{c}_{j,\alpha\sigma,n'} \\ &= -t_{\text{hop}} \sum_{(ij)} \sum_{\alpha\sigma} c_{i,\alpha\sigma}^\dagger c_{j,\alpha\sigma} P_{i,n-1} P_{j,n'}. \end{aligned} \quad (\text{A4})$$

It can be seen from Eqs. (A3) and (A4) that the kinetic term is divided into different sectors with fixed particle numbers at sites i and j . With this notation we can proceed to perform a rotating-frame transformation generated by the term of the Hubbard Hamiltonian with the largest energy scale, H_U . We thus arrive at the rotating frame Hamiltonian H_{rot} given by

$$H_{\text{rot}} = -H_U + e^{iH_U t} H e^{-iH_U t}. \quad (\text{A5})$$

The last term in the above expression can be expanded using the Baker-Campbell-Hausdorff (BCH) formula, which requires the evaluation of $[H_U, H]$. Since H_U commutes with all the other terms except H_{hop} , the commutator can be reduced to $[H_U, H_{\text{hop}}]$, which evaluates to

$$\begin{aligned} [H_U, H_{\text{hop}}] &= \sum_{n,n'} [H_U, H_{\text{hop},nn'}] \\ &= \sum_{n,n'} (n - n') U H_{\text{hop},nn'}. \end{aligned} \quad (\text{A6})$$

We can further simplify the notation by introducing a new index $m = n - n'$, with which the commutator can be written as

$$\begin{aligned} [H_U, H_{\text{hop}}] &= \sum_m m U \left(\sum_n H_{\text{hop},n n-m} \right) \\ &\equiv \sum_m m U H_{\text{hop},m}, \end{aligned} \quad (\text{A7})$$

where m can take values from -3 to 3 with the constraint $4 > n - m \geq 0$ and $m \neq 0$. With these results, one can derive

the following expression for H_{rot} :

$$H_{\text{rot}} = H_\mu + \sum_m H_{\text{hop},m} e^{imUt}. \quad (\text{A8})$$

This is a time-periodic Hamiltonian with frequency U . By averaging out the high-frequency dynamics, we obtain the low-energy effective Hamiltonian describing the nonstroboscopic dynamics, which is given by

$$H_{\text{eff}} = H_\mu + H_{\text{hop},0} + H_{\text{hop},2/U}^2 + O(t_{\text{hop}}^3/U), \quad (\text{A9})$$

$$H_{\text{hop},0} = -t_{\text{hop}} \sum_{(ij)n} \sum_{\alpha\sigma} c_{i,\alpha\sigma}^\dagger c_{j,\alpha\sigma} P_{i,n-1} P_{j,n} + (i \leftrightarrow j), \quad (\text{A10})$$

$$H_{\text{hop},2/U}^2 = \sum_{m \neq 0} \frac{H_{\text{hop},m} H_{\text{hop},-m}}{mU}. \quad (\text{A11})$$

By inserting the expressions for $H_{\text{hop},m}$ and neglecting three-site terms, we arrive at

$$\begin{aligned} H_{\text{hop},2/U}^2 &= \frac{t_{\text{hop}}^2}{U} \sum_{(ij)} \sum_n \left(\sum_{\substack{\alpha,\alpha' \\ \sigma,\sigma'}} \sum_{\alpha\sigma \neq \alpha'\sigma'} c_{i,\alpha\sigma}^\dagger c_{i,\alpha'\sigma'}^\dagger c_{j,\alpha'\sigma'} c_{j,\alpha\sigma} \right) \\ &\quad \times P_{i,n-2} P_{j,n} \\ &\quad + \frac{t_{\text{hop}}^2}{U} \sum_{(ij)} \sum_{n,m} \frac{1}{m} \left(n_i - \sum_{\substack{\alpha,\alpha' \\ \sigma,\sigma'}} c_{i,\alpha\sigma}^\dagger c_{i,\alpha'\sigma'}^\dagger c_{j,\alpha'\sigma'} c_{j,\alpha\sigma} \right) \\ &\quad \times P_{i,n} P_{j,n-m-1} + (i \leftrightarrow j). \end{aligned} \quad (\text{A12})$$

In the completely photodoped two-orbital system, each site is either triply occupied (triplons) or singly occupied (singlons). Therefore, we project the effective Hamiltonian to the triplon-singlon subspace by choosing appropriate values for n and m to obtain the projection operators $P_{i,1}$ ($P_{j,1}$) and $P_{i,3}$ ($P_{j,3}$). Then the projected Hamiltonian $H_{\text{hop},2/U}^2$ can be divided into three parts—the triplon-triplon part $H_{\text{hop},2/U}^{tt}$ ($P_{i,3} P_{j,3}$), singlon-singlon part $H_{\text{hop},2/U}^{ss}$ ($P_{i,1} P_{j,1}$), and singlon-triplon part $H_{\text{hop},2/U}^{st}$ ($P_{i,1} P_{j,3}$). Note that the three-site terms do not contribute (within the triplon-singlon subspace) in a completely photodoped system. The first term on the right hand side of Eq. (A12) can be written in terms of η^+ and η^- , whereas the second term can be decomposed into Kugel-Khomskii spin-orbital terms [48]. To achieve the Kugel-Khomskii decomposition we write the operator $c_{i\alpha\sigma}^\dagger c_{i\alpha'\sigma'}$ as the product τs (where τ is the orbital-pseudospin and s is the spin operator) with the following rule:

$$\begin{aligned} (\alpha, \alpha') &= (1, 1) \rightarrow \frac{1}{2} + \tau^z, & (2, 2) &\rightarrow \frac{1}{2} - \tau^z, \\ (1, 2) &\rightarrow \tau^+, & (2, 1) &\rightarrow \tau^-, \\ (\sigma, \sigma') &= (\uparrow, \uparrow) \rightarrow \frac{1}{2} + s^z, & (\downarrow, \downarrow) &\rightarrow \frac{1}{2} - s^z, \\ (\uparrow, \downarrow) &\rightarrow s^+, & (\downarrow, \uparrow) &\rightarrow s^-. \end{aligned} \quad (\text{A13})$$

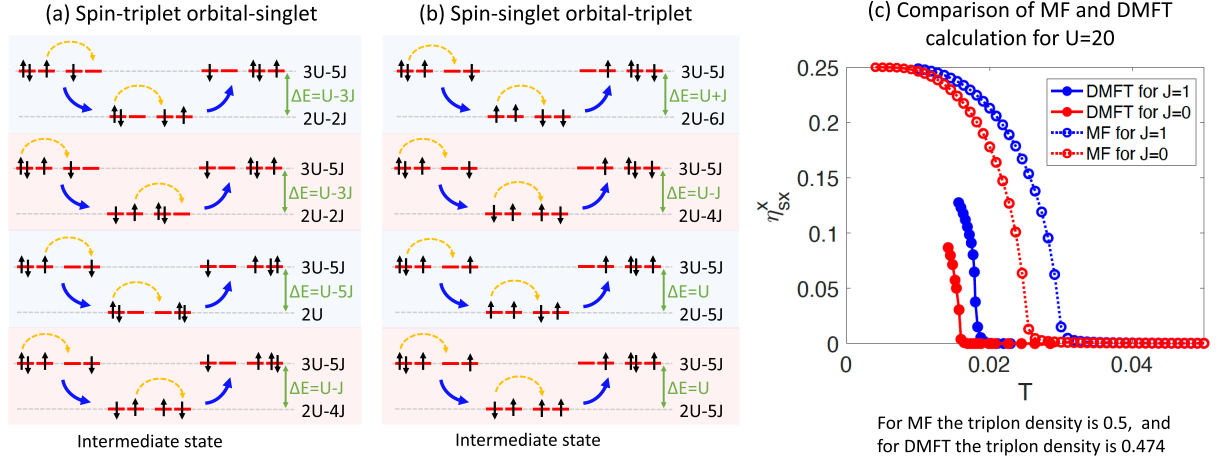


FIG. 6. Various second order hopping processes contributing to η_{sx} and η_{ox} pairing. (a) $c_{1\uparrow}^\dagger c_{2\uparrow}^\dagger$ spin-triplet hopping and (b) $c_{1\uparrow}^\dagger c_{1\downarrow}^\dagger$ spin-singlet hopping. (c) MF and DMFT η_{sx}^x superconducting order for $U = 20$ and for Hund coupling $J = 0$ and 1. Both MF (for triplon density 0.474) and DMFT (for triplon density 0.5) show an enhancement of the η_{sx}^x order upon inclusion of a Hund coupling $J > 0$.

This leads us to the expression for the effective Hamiltonian for $J = 0$, which is shown in Eqs. (6) and (7) of the main manuscript:

$$H_{t_{\text{hop}}^2/U}^{st} = -\frac{4t_{\text{hop}}^2}{U} \sum_{(ij),\alpha} (\eta_{i\alpha}^+ \eta_{j\alpha}^- + \eta_{i\alpha}^- \eta_{j\alpha}^+) - \frac{4t_{\text{hop}}^2}{3U} \sum_{(ij)} \left(\frac{1}{2} + 2s_i \cdot s_j \right) \left(\frac{1}{2} + 2\tau_i \cdot \tau_j \right), \quad (\text{A14})$$

$$H_{t_{\text{hop}}^2/U}^{ss(tr)} = \frac{2t_{\text{hop}}^2}{U} \sum_{(ij)} \left(\frac{1}{2} + 2s_i \cdot s_j \right) \left(\frac{1}{2} + 2\tau_i \cdot \tau_j \right). \quad (\text{A15})$$

The $J \neq 0$ case can be analyzed by noting that in Eq. (A14) the η terms come from second order hopping processes, where the energy difference between the initial state and the intermediate state depends on J . In the absence of Hund coupling ($J = 0$), all the η superconducting pairings are degenerate, since all the intermediate states differ by the same local energy $\Delta E = U$ from the initial and final state. The inclusion of Hund coupling lifts this degeneracy, as the intermediate doublon states are no longer degenerate. As shown in Fig. 6(a), for $J > 0$ the spin-triplet orbital-singlet η_{sx} pairing has intermediate doublon states which differ by the local energy $\Delta E = U - 2J, U - 3J, U - 5J$ from the initial state (consisting of a singlon-triplon pair with local energy $3U - 5J$). In Fig. 6(a), we only show the intermediate state for the hopping process $c_{1\uparrow}^\dagger c_{2\uparrow}^\dagger$. It can be easily seen that all the other processes involved in η_{sx} pairing have the same energy configurations. Taking into account all the intermediate states in second order perturbation theory, the effective \tilde{U}_{sx} for spin-triplet η_{sx} pairing can be calculated as

$$\frac{1}{\tilde{U}_{sx}} = \frac{1}{4} \left(\frac{1}{U-J} + \frac{2}{U-3J} + \frac{1}{U-5J} \right). \quad (\text{A16})$$

On the other hand, orbital-triplet spin-singlet η_{ox} pairing has intermediate doublon states with local energy differences $\Delta E = U - J, U, U + J$ [see Fig. 6(b)] and thus the effective

\tilde{U}_{ox} is given by

$$\frac{1}{\tilde{U}_{ox}} = \frac{1}{4} \left(\frac{1}{U-J} + \frac{2}{U} + \frac{1}{U+J} \right). \quad (\text{A17})$$

It follows from these expressions that $J > 0$ favors spin-triplet η_{sx} pairing, because the lower \tilde{U} results in a larger exchange coupling. Similarly, $J < 0$ favors orbital-triplet η_{ox} pairing.

APPENDIX B: NONEQUILIBRIUM SPECTRAL FUNCTION

The nonequilibrium single-particle spectra of multiorbital systems with Hund coupling can be very different from the equilibrium counterpart. In equilibrium, the half filled system without Hund coupling ($J = 0$) has a band gap of U between the lower and upper Hubbard band. Near the atomic limit ($U \gg t_{\text{hop}}$), for $J > 0$, the two dominant Hubbard subbands are separated by $U + J$, while for $J < 0$ the band gap is $U + 5|J|$. In nonequilibrium photodoped systems, the triplon sites have a local energy $3U - 5J$ and the removal of an electron from a triplon site can produce doublons with interaction energy $U, U - 2J$, or $U - 3J$. Similarly, taking into account the chemical potential term, a singlon can gain local energy by the addition of an electron. Thus in the nonequilibrium system, the splitting between the Hubbard bands, estimated as $E_{\text{loc}}^{N=3} + E_{\text{loc}}^{N=1} - 2E_{\text{loc}}^{N=2}$, is expected to cover the energy range from approximately $U - 5J$ to $U + J$.

Consistent with this expectation, in Figs. 1(b) and 1(c), we see a smaller separation between the Hubbard bands for $J = 1$ than for $J = -1$. Here, the substructures associated with different doublon states are broadened due to the kinetic term. By reducing the hopping t_{hop} , the corresponding peaks can be made sharp. In Fig. 7(a), we plot the spectra for $U = 20, J = 1, t_{\text{hop}} = 0.3$. One can now clearly identify the features produced by the different doublon states upon removal of an electron from a triplon (upper Hubbard band) or addition of an electron to a singlon (lower Hubbard band). As a result of these peaks, the gap shrinks, compared to $J = 0$. Similarly, Fig. 7(b) shows that, for $J = -1$, the additional peaks induced

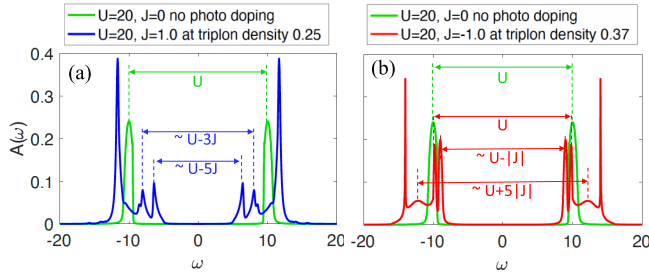


FIG. 7. Nonequilibrium spectra for (a) $U = 20, J = 1$ and (b) $U = 20, J = -1$. Both spectra are obtained for a reduced $t_{\text{hop}} = 0.3$ and are compared with the undoped equilibrium spectrum for $U = 20, J = 0$ (green). For $J > 0$ [panel (a)], additional peaks appear with an energy separation of approximately $U - 5J$ and $U - 3J$, resulting in a smaller gap. In panel (b), for $J < 0$, a prominent feature with an energy separation of approximately $U + 5|J|$ appears, resulting in an overall larger separation of the Hubbard bands.

by photodoping lead to a broadening and enhanced splitting of the Hubbard bands.

APPENDIX C: MEAN-FIELD DECOUPLING

We perform the mean-field (MF) decoupling on the effective model given by Eqs. (A14) and (A15), which (neglecting a constant term) yields

$$H_{t_{\text{hop}}^2/U}^{ts, \text{MF}} = -\frac{4t_{\text{hop}}^2}{U} \sum_{(ij)} \left[\sum_{\alpha} (\langle \eta_{i\alpha}^+ \rangle \eta_{j\alpha}^- + \langle \eta_{i\alpha}^- \rangle \eta_{j\alpha}^+) - \frac{1}{3} (\langle s_i \rangle \cdot s_j + \langle \tau_i \rangle \cdot \tau_j + 4 \langle s_i \tau_i \rangle s_j \tau_j) \right] + (i \rightarrow j),$$

$$H_{t_{\text{hop}}^2/U}^{ss(tt), \text{MF}} = \frac{2t_{\text{hop}}^2}{U} \sum_{(ij)} [\langle s_i \rangle \cdot s_j + \langle \tau_i \rangle \cdot \tau_j + 4 \langle s_i \tau_i \rangle s_j \tau_j] + (i \rightarrow j), \quad (\text{C1})$$

where the spin-orbital composite order $s_i \tau_i$ can be defined as a tensor $(s_i \tau_i)^{\mu\nu} = \sum_{\alpha\sigma} \sum_{\alpha'\sigma'} c_{i,\alpha\sigma}^{\dagger} \sigma_{\sigma\sigma'}^{\mu} \tau_{\alpha\alpha'}^{\nu} c_{i,\alpha'\sigma'}$. This MF Hamiltonian can be solved self-consistently for η order. We calculate the MF η order for the extremely photodoped (triplon density 0.5) system. As mentioned earlier, in this limit, each site is either a triplon or a singlon. So, all the operators used in the MF Hamiltonian can be written in the triplon-singlon basis. First, we note that there are four triplons and four singlons denoted by

$$\begin{aligned} |t_{1\uparrow}\rangle_i &= t_{i,1\uparrow}^{\dagger} |0\rangle_i = c_{i,1\uparrow}^{\dagger} c_{i,2\uparrow}^{\dagger} c_{i,2\downarrow}^{\dagger} |0\rangle_i, \\ |t_{1\downarrow}\rangle_i &= t_{i,1\downarrow}^{\dagger} |0\rangle_i = c_{i,1\downarrow}^{\dagger} c_{i,2\uparrow}^{\dagger} c_{i,2\downarrow}^{\dagger} |0\rangle_i, \\ |t_{2\uparrow}\rangle_i &= t_{i,2\uparrow}^{\dagger} |0\rangle_i = c_{i,1\uparrow}^{\dagger} c_{i,1\downarrow}^{\dagger} c_{i,2\uparrow}^{\dagger} |0\rangle_i, \\ |t_{2\downarrow}\rangle_i &= t_{i,2\downarrow}^{\dagger} |0\rangle_i = c_{i,1\downarrow}^{\dagger} c_{i,1\uparrow}^{\dagger} c_{i,2\downarrow}^{\dagger} |0\rangle_i, \end{aligned} \quad (\text{C2})$$

$$\begin{aligned} |s_{1\uparrow}\rangle_i &= s_{i,1\uparrow}^{\dagger} |0\rangle_i = c_{i,1\uparrow}^{\dagger} |0\rangle_i, \\ |s_{1\downarrow}\rangle_i &= s_{i,1\downarrow}^{\dagger} |0\rangle_i = c_{i,1\downarrow}^{\dagger} |0\rangle_i, \\ |s_{2\uparrow}\rangle_i &= s_{i,2\uparrow}^{\dagger} |0\rangle_i = c_{i,2\uparrow}^{\dagger} |0\rangle_i, \\ |s_{2\downarrow}\rangle_i &= s_{i,2\downarrow}^{\dagger} |0\rangle_i = c_{i,2\downarrow}^{\dagger} |0\rangle_i, \end{aligned} \quad (\text{C3})$$

where $|t_{\alpha\sigma}\rangle_i$ denotes the triplon state, $|s_{\alpha\sigma}\rangle_i$ denotes the singlon state, and $|0\rangle_i$ is the vacuum state at site i . Now, we can define the triplon basis as $\mathcal{T}^{\dagger} = (t_{1\uparrow}^{\dagger}, t_{1\downarrow}^{\dagger}, t_{2\uparrow}^{\dagger}, t_{2\downarrow}^{\dagger})$ and the singlon basis as $\mathcal{S}^{\dagger} = (s_{1\uparrow}^{\dagger}, s_{1\downarrow}^{\dagger}, s_{2\uparrow}^{\dagger}, s_{2\downarrow}^{\dagger})$. The triplon-singlon basis is then written as $\psi^{\dagger} = (\mathcal{T}^{\dagger}, \mathcal{S}^{\dagger})$, which we use to write the MF operators. For example, the η operator takes a singlon and converts it into a triplon and vice versa. So, η operators correspond to off-diagonal block matrices. On the other hand, all the spin and orbital operators are block diagonal in this basis.

Figure 6(c) shows the MF results for the order parameter $\eta_{sx}^x = \text{Re}[\eta_{sx}^{\dagger}]$ as a function of temperature T for $U = 20$ and triplon density 0.5. In the absence of Hund coupling ($J = 0$), the MF SC transition temperature is $T_c^{\text{MF}} \sim 0.026$ (red dashed line), whereas the DMFT calculation shows a SC transition temperature $T_c^{\text{DMFT}} \sim 0.018$ (red line) for triplon density 0.474. This overestimation may be due to the fact that we cannot reach the extreme doping (triplon density 0.5) limit in DMFT and also because the MF calculation is based on an effective model which is valid in the $U \gg t$ limit. The MF treatment also neglects temporal fluctuations and the coupling to fermion baths, which may contribute to the comparatively lower T_c in the DMFT calculations. However, consistent with the DMFT results, we observe that the inclusion of a $J > 0$ Hund coupling term favors the spin-triplet orbital-singlet η order, as shown in Fig. 6(c), where T_c^{MF} is enhanced (blue dashed line). The DMFT calculation shows the same trend (solid blue line).

APPENDIX D: DMFT CALCULATIONS

As mentioned in the main text, in the DMFT calculations the Green's function $G(t, t')$ and the hybridization function $\Delta(t, t')$ are expressed in the Nambu basis. In order to measure the spin-triplet superconducting order, we introduce the spinor $\psi^{\dagger} = (c_{1\uparrow}^{\dagger}, c_{2\uparrow}^{\dagger}, c_{1\downarrow}^{\dagger}, c_{2\downarrow}^{\dagger})$ so that the hybridization function and the Green's function can be written in this basis as 4×4 matrices

$$\Delta(t, t') = \begin{bmatrix} \Delta_{1\uparrow 1\uparrow}^{c^{\dagger}c} & \Delta_{1\uparrow 2\uparrow}^{c^{\dagger}c^{\dagger}} & 0 & \Delta_{1\uparrow 2\downarrow}^{c^{\dagger}c^{\dagger}} \\ \Delta_{2\uparrow 1\uparrow}^{cc} & \Delta_{2\uparrow 2\uparrow}^{cc^{\dagger}} & \Delta_{2\uparrow 1\downarrow}^{cc} & 0 \\ 0 & \Delta_{1\downarrow 2\uparrow}^{c^{\dagger}c^{\dagger}} & \Delta_{1\downarrow 1\downarrow}^{c^{\dagger}c} & \Delta_{1\downarrow 2\downarrow}^{c^{\dagger}c^{\dagger}} \\ \Delta_{2\downarrow 1\uparrow}^{cc} & 0 & \Delta_{2\downarrow 1\downarrow}^{cc} & \Delta_{2\downarrow 2\downarrow}^{cc^{\dagger}} \end{bmatrix},$$

$$G(t, t') = \begin{bmatrix} G_{1\uparrow 1\uparrow}^{cc^{\dagger}} & G_{1\uparrow 2\uparrow}^{cc} & 0 & G_{1\uparrow 2\downarrow}^{cc} \\ G_{2\uparrow 1\uparrow}^{c^{\dagger}c^{\dagger}} & G_{2\uparrow 2\uparrow}^{c^{\dagger}c} & G_{2\uparrow 1\downarrow}^{c^{\dagger}c^{\dagger}} & 0 \\ 0 & G_{1\downarrow 2\uparrow}^{cc} & G_{1\downarrow 1\downarrow}^{cc^{\dagger}} & G_{1\downarrow 2\downarrow}^{cc} \\ G_{2\downarrow 1\uparrow}^{c^{\dagger}c^{\dagger}} & 0 & G_{2\downarrow 1\downarrow}^{c^{\dagger}c^{\dagger}} & G_{2\downarrow 2\downarrow}^{c^{\dagger}c} \end{bmatrix}.$$

The DMFT self-consistency equations in this Nambu basis can be written as $\Delta(t, t') = t_0^2 \gamma G(t, t') \gamma$. For uniform superconducting order γ is a diagonal matrix given by $\gamma = \text{diag}(1, -1, 1, -1)$ and for staggered η superconducting order γ is a unity matrix $\gamma = \text{diag}(1, 1, 1, 1)$. Please note that to measure the spin-triplet order we assume there is no intraorbital superconducting order like $c_{\alpha\uparrow}^{\dagger} c_{\alpha\downarrow}^{\dagger}$. In a

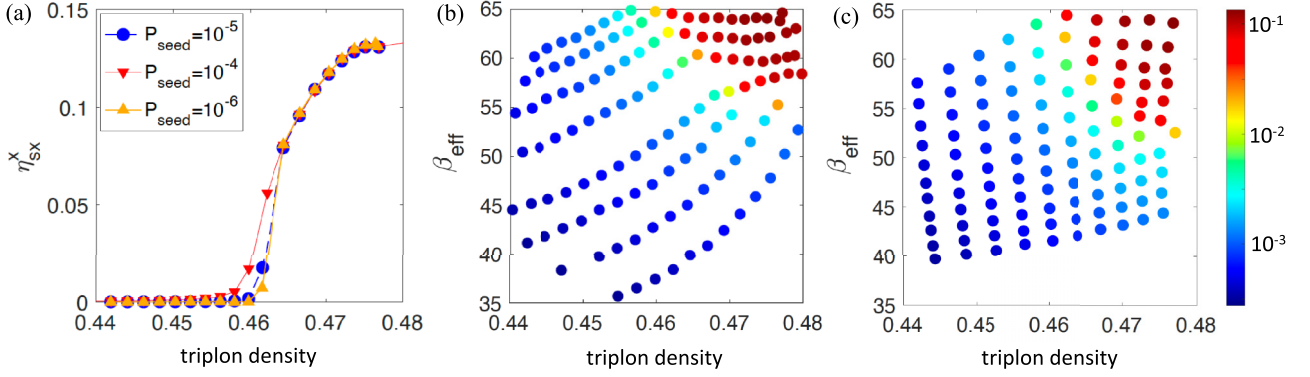


FIG. 8. (a) Spin-triplet orbital-singlet superconducting order η_{sx}^x as a function of triplon density for different seed fields P_{seed} for $U = 20$, $J = 1$, $\Gamma = 0.02$, and $\beta_{\text{eff}} = 60$. In the superconducting state (triplon density above 0.463) the values of the order parameter become essentially independent of the seed field, which indicates a spontaneous symmetry breaking. Panels (b) and (c) show the phase diagrams in the β_{eff} and triplon density space for $U = 20$ and $J = 1$. The effective temperature β_{eff} is controlled by tuning two different parameters—the coupling to the fermion bath ($\Gamma = 0.01$ to 0.03) in (b) and the temperature of the fermion bath (keeping the coupling constant at $\Gamma = 0.02$) in (c), whereas the triplon density is mainly controlled by the chemical potential of the fermion baths μ_b . The color map indicates the order parameter.

similar manner, for measuring the spin-singlet order, we assume no interorbital pairing and write the hybridization function and Green's function in the spinor basis $\psi^\dagger = (c_{1\uparrow}^\dagger, c_{1\downarrow}^\dagger, c_{2\uparrow}^\dagger, c_{2\downarrow}^\dagger)$. For the derivation of these DMFT equations, one can follow Ref. [50].

To measure a specific superconducting order, we apply a small seed field P_{seed} and couple it to the superconducting order and keep it on during the self-consistent calculation DMFT calculation. In a symmetry-broken state, except close to the phase transition point, the order parameter should not strongly depend on the seed field. We demonstrate this in Fig. 8(a), where seed fields of different orders of magnitude (10^{-4} , 10^{-5} , 10^{-6}) were applied to measure η_{sx}^x for $U = 20$ and $J = 1$. The value of the order parameter η_{sx}^x is essentially independent of the seed field above triplon density 0.463, which indicates the existence of a symmetry-broken state. We have also checked that the value of the order parameter remains fixed even if we switch off the seed field after a certain number of DMFT iterations. For triplon densities below 0.463, the order parameter is reduced if the seed field is reduced, suggestive of a normal state. Our data indicate a discontinuous transition from the normal to the superconducting phase at the given effective temperature ($T_{\text{eff}} = 1/60$).

The nonequilibrium steady state corresponds to a partially thermalized photodoped state, where the electrons are thermalized within each Hubbard band. Such a state should be described by a well-defined effective temperature which we can find by comparing the distribution function of the electrons in each Hubbard band to an appropriately shifted Fermi distribution function. In order to demonstrate that the nonequilibrium state is indeed described by an effective temperature $T_{\text{eff}} = 1/\beta_{\text{eff}}$, we cool the system by varying different parameters. Our calculation shows that the steady state is described by the same order parameter at a fixed β_{eff} and it does not depend on how this temperature is achieved. Figures 8(b) and 8(c) show the phase diagram of photodoped systems with $U = 20$ and $J = 1$, obtained by tuning the coupling to the fermion bath [Fig. 8(b)] and by tuning the temperature of the fermion bath [Fig. 8(c)]. It can be seen that the phase diagram

is essentially independent of the tuning parameter used to cool down the system.

Finally, we show in Fig. 9 the phase diagram for a photodoped system with $U = 20$ and $\beta_{\text{eff}} = 60$ in the space spanned by the Hund coupling J and triplon density. Our calculation shows that indeed η pairing is favored as we increase the Hund coupling J , which is qualitatively consistent with the MF result. In Fig. 9 we plot both the spin-singlet orbital-triplet order η_{ox}^x [Fig. 9(a)] and the spin-triplet orbital-singlet order η_{sx}^x [Fig. 9(b)]. We observe that both superconducting orders are stabilized in the presence of a nonzero J . But the η_{sx}^x order has higher values for $J > 0$. This suggests that, for positive values of J , the dominant superconducting order is given by η_{sx} , whereas for negative J the orbital-triplet order η_{ox} is the dominant order. The resulting phase diagram is consistent with the fact that the $J < 0$ model can be mapped qualitatively to the $J > 0$ model by flipping the spin and orbital degrees of freedom as $c_{i,1\downarrow} \rightarrow c_{i,2\uparrow}$ and $c_{i,2\uparrow} \rightarrow c_{i,1\downarrow}$ [53]. After this transformation the density-density interaction terms of the Hamiltonian become

$$H_U = \frac{\tilde{U}}{2} \sum_i \sum_{\alpha=1,2} \sum_{\sigma\sigma'} n_{i,\alpha\sigma} n_{i,\alpha\sigma'}, \quad (\text{D1})$$

$$\begin{aligned} H_J &= -J \sum_{i,\sigma} n_{i,1\sigma} n_{i,2\bar{\sigma}} - 3J \sum_{i,\sigma} n_{i,1\sigma} n_{i,2\sigma} \\ &= |J| \sum_{i,\sigma} n_{i,1\sigma} n_{i,2\bar{\sigma}} + 3|J| \sum_{i,\sigma} n_{i,1\sigma} n_{i,2\sigma}. \end{aligned} \quad (\text{D2})$$

Defining $\tilde{U} = U - 3J = U + 3|J|$, the intraorbital repulsion for negative J becomes $\tilde{U} = U + 3|J|$, the interorbital repulsion for same spins $\tilde{U} - 3|J| = U$, and the interorbital repulsion for opposite spins $\tilde{U} - |J| = U + 2|J|$. Moreover, since the spin and orbital degrees of freedom are exchanged in this transformation, the superconducting order parameter changes as

$$(c_{1\uparrow}^\dagger c_{2\uparrow}^\dagger - c_{1\downarrow}^\dagger c_{2\downarrow}^\dagger) \rightarrow (c_{1\uparrow}^\dagger c_{1\downarrow}^\dagger - c_{2\uparrow}^\dagger c_{2\downarrow}^\dagger). \quad (\text{D3})$$

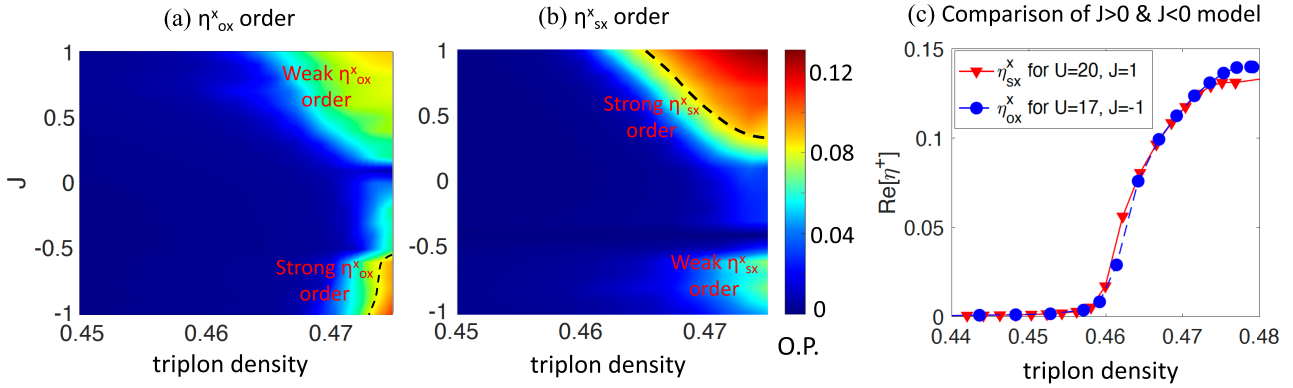


FIG. 9. Nonequilibrium phase diagrams for η superconductivity in the space of triplon density and Hund coupling. The orbital-triplet order η_{ox}^x is plotted in (a) and spin-triplet order η_{sx}^x is plotted in (b), with the color map indicating the order parameter (O.P.). η_{sx}^x dominates the $J > 0$ region, while η_{ox}^x dominates the $J < 0$ region. The qualitative equivalence of the $J > 0$ and $J < 0$ models is shown in panel (c) by plotting η_{sx}^x for $U = 20, J = 1$ and η_{ox}^x for $\tilde{U} = U + 3|J| = 20, J = -1$ as a function of the triplon density at $\beta_{\text{eff}} = 60$.

Thus we expect an orbital-triplet η order for $J < 0$. The higher effective \tilde{U} explains the smaller superconducting region in the phase diagram for negative J . This qualitative equivalence of the $J > 0$ and $J < 0$ models is further verified in Fig. 9(c), where we compare the η_{sx}^x order for

the $U = 20, J = 1$ model to the η_{ox}^x order for the $U = 17, J = -1$ ($\tilde{U} = 20$) model as a function of triplon density at $\beta_{\text{eff}} = 60$. Both curves (red and blue) almost fall on top of each other, which demonstrates the validity of the mapping.

- [1] D. N. Basov, R. D. Averitt, and D. Hsieh, *Nat. Mater.* **16**, 1077 (2017).
- [2] C. Giannetti, M. Capone, D. Fausti, M. Fabrizio, F. Parmigiani, and D. Mihailovic, *Adv. Phys.* **65**, 58 (2016).
- [3] T. Oka and S. Kitamura, *Annu. Rev. Condens. Matter Phys.* **10**, 387 (2019).
- [4] A. de la Torre, D. M. Kennes, M. Claassen, S. Gerber, J. W. McIver, and M. A. Sentef, *Rev. Mod. Phys.* **93**, 041002 (2021).
- [5] H. Ichikawa, S. Nozawa, T. Sato, A. Tomita, K. Ichiyani, M. Chollet, L. Guerin, N. Dean, A. Cavalleri, S.-i. Adachi *et al.*, *Nat. Mater.* **10**, 101 (2011).
- [6] L. Stojchevska, I. Vaskivskiy, T. Mertelj, P. Kusar, D. Svetin, S. Brazovskii, and D. Mihailovic, *Science* **344**, 177 (2014).
- [7] E. Dagotto, *Science* **309**, 257 (2005).
- [8] S. Mor, M. Herzog, D. Golez, P. Werner, M. Eckstein, N. Katayama, M. Nohara, H. Takagi, T. Mizokawa, C. Monney, and J. Stahler, *Phys. Rev. Lett.* **119**, 086401 (2017).
- [9] T. Li, A. Patz, L. Mouchliadis, J. Yan, T. A. Lograsso, I. E. Perakis, and J. Wang, *Nature (London)* **496**, 69 (2013).
- [10] R. Mikhaylovskiy, E. Hendry, A. Secchi, J. H. Mentink, M. Eckstein, A. Wu, R. Pisarev, V. Kruglyak, M. Katsnelson, T. Rasing *et al.*, *Nat. Commun.* **6**, 8190 (2015).
- [11] A. Kirilyuk, A. V. Kimel, and T. Rasing, *Rev. Mod. Phys.* **82**, 2731 (2010).
- [12] D. Fausti, R. I. Tobey, N. Dean, S. Kaiser, A. Dienst, M. C. Hoffmann, S. Pyon, T. Takayama, H. Takagi, and A. Cavalleri, *Science* **331**, 189 (2011).
- [13] M. Mitran, A. Cantaluppi, D. Nicoletti, S. Kaiser, A. Perucchi, S. Lupi, P. Di Pietro, D. Pontiroli, M. Ricco, S. R. Clark *et al.*, *Nature (London)* **530**, 461 (2016).
- [14] P. Werner, N. Tsuji, and M. Eckstein, *Phys. Rev. B* **86**, 205101 (2012).
- [15] A. Ono and S. Ishihara, *Phys. Rev. Lett.* **119**, 207202 (2017).
- [16] J. Li, H. U. R. Strand, P. Werner, and M. Eckstein, *Nat. Commun.* **9**, 4581 (2018).
- [17] P. Werner and Y. Murakami, *Phys. Rev. B* **102**, 241103(R) (2020).
- [18] T. Kaneko, T. Shirakawa, S. Sorella, and S. Yunoki, *Phys. Rev. Lett.* **122**, 077002 (2019).
- [19] P. Werner, J. Li, D. Golez, and M. Eckstein, *Phys. Rev. B* **100**, 155130 (2019).
- [20] J. Tindall, B. Buca, J. R. Coulthard, and D. Jaksch, *Phys. Rev. Lett.* **123**, 030603 (2019).
- [21] J. Li, D. Golez, P. Werner, and M. Eckstein, *Phys. Rev. B* **102**, 165136 (2020).
- [22] P. Werner and Y. Murakami, *Phys. Rev. B* **104**, L201101 (2021).
- [23] Y. Murakami, S. Takayoshi, T. Kaneko, A. M. Läuchli, and P. Werner, *Phys. Rev. Lett.* **130**, 106501 (2023).
- [24] A. Takahashi, H. Gomi, and M. Aihara, *Phys. Rev. B* **66**, 115103 (2002).
- [25] A. Rosch, D. Rasch, B. Binz, and M. Vojta, *Phys. Rev. Lett.* **101**, 265301 (2008).
- [26] Y. Murakami, S. Takayoshi, T. Kaneko, Z. Sun, D. Golež, A. J. Millis, and P. Werner, *Commun. Phys.* **5**, 23 (2022).
- [27] T. Oka and H. Aoki, *Phys. Rev. B* **79**, 081406(R) (2009).
- [28] Y. H. Wang, H. Steinberg, P. Jarillo-Herrero, and N. Gedik, *Science* **342**, 453 (2013).
- [29] S. Iwai, M. Ono, A. Maeda, H. Matsuzaki, H. Kishida, H. Okamoto, and Y. Tokura, *Phys. Rev. Lett.* **91**, 057401 (2003).
- [30] R. Sensarma, D. Pekker, E. Altman, E. Demler, N. Strohmaier, D. Greif, R. Jördens, L. Tarruell, H. Moritz, and T. Esslinger, *Phys. Rev. B* **82**, 224302 (2010).
- [31] M. Eckstein and P. Werner, *Phys. Rev. B* **84**, 035122 (2011).

- [32] N. Strohmaier, D. Greif, R. Jördens, L. Tarruell, H. Moritz, T. Esslinger, R. Sensarma, D. Pekker, E. Altman, and E. Demler, *Phys. Rev. Lett.* **104**, 080401 (2010).
- [33] Z. Lenarčič and P. Prelovšek, *Phys. Rev. B* **90**, 235136 (2014).
- [34] N. Maeshima and K. Yonemitsu, *J. Phys. Soc. Jpn.* **74**, 2671 (2005).
- [35] D. Golež, J. Bonca, L. Vidmar, and S. A. Trugman, *Phys. Rev. Lett.* **109**, 236402 (2012).
- [36] K. Shinjo and T. Tohyama, *Phys. Rev. B* **96**, 195141 (2017).
- [37] M. Sandri and M. Fabrizio, *Phys. Rev. B* **88**, 165113 (2013).
- [38] M. Eckstein and P. Werner, *Phys. Rev. Lett.* **110**, 126401 (2013).
- [39] N. Tancogne-Dejean, M. A. Sentef, and A. Rubio, *Phys. Rev. Lett.* **121**, 097402 (2018).
- [40] J. Rincon, E. Dagotto, and A. E. Feiguin, *Phys. Rev. B* **97**, 235104 (2018).
- [41] K. Zawadzki and A. E. Feiguin, *Phys. Rev. B* **100**, 195124 (2019).
- [42] M. Schüler, U. De Giovannini, H. Hübener, A. Rubio, M. A. Sentef, T. P. Devereaux, and P. Werner, *Phys. Rev. X* **10**, 041013 (2020).
- [43] N. Bittner, D. Golez, M. Casula, and P. Werner, *Phys. Rev. B* **104**, 115138 (2021).
- [44] E. Peretto, Y. Pavlyukh, and G. Stefanucci, *Phys. Rev. Lett.* **128**, 016801 (2022).
- [45] P. Werner, M. Eckstein, M. Müller, and G. Refael, *Nat. Commun.* **10**, 5556 (2019).
- [46] J. Li and M. Eckstein, *Phys. Rev. B* **103**, 045133 (2021).
- [47] J. Li, M. Müller, A. J. Kim, A. Läuchli, and P. Werner, *Phys. Rev. B* **107**, 205115 (2023).
- [48] K. I. Kugel and D. I. Khomskii, *Sov. Phys. Usp.* **25**, 231 (1982).
- [49] G. Khaliullin and V. Oudovenko, *Phys. Rev. B* **56**, R14243(R) (1997).
- [50] P. Werner, H. U. R. Strand, S. Hoshino, Y. Murakami, and M. Eckstein, *Phys. Rev. B* **97**, 165119 (2018).
- [51] N. Dasari, J. Li, P. Werner, and M. Eckstein, *Phys. Rev. B* **103**, L201116 (2021).
- [52] S. Hoshino and P. Werner, *Phys. Rev. B* **93**, 155161 (2016).
- [53] K. Steiner, S. Hoshino, Y. Nomura, and P. Werner, *Phys. Rev. B* **94**, 075107 (2016).
- [54] H. Aoki, N. Tsuji, M. Eckstein, M. Kollar, T. Oka, and P. Werner, *Rev. Mod. Phys.* **86**, 779 (2014).
- [55] M. Eckstein and P. Werner, *Phys. Rev. B* **82**, 115115 (2010).
- [56] S.-S. B. Lee, J. von Delft, and A. Weichselbaum, *Phys. Rev. B* **96**, 245106 (2017).